

Received August 25, 2019, accepted September 3, 2019, date of publication September 10, 2019,
date of current version September 25, 2019.

Digital Object Identifier 10.1109/ACCESS.2019.2940255

Low-Rank Tensor Completion via Tensor Nuclear Norm With Hybrid Smooth Regularization

XI-LE ZHAO^{ID1}, XIN NIE¹, YU-BANG ZHENG^{ID1}, TENG-YU JI^{ID2}, AND TING-ZHU HUANG^{ID1}

¹School of Mathematical Sciences/Research Center for Image and Vision Computing, University of Electronic Science and Technology of China, Chengdu 611731, China

²School of Science, Northwestern Polytechnical University, Xi'an 710072, China

Corresponding author: Xin Nie (niexin_7@163.com)

This work was supported in part by the NSFC under Grant 61876203 and Grant 61772003, and in part by the Fundamental Research Funds for the Central Universities under Grant 31020180QD126.

ABSTRACT As a convex surrogate of tensor multi rank, recently the tensor nuclear norm (TNN) obtains promising results in the tensor completion. However, only considering the low-tubal-rank prior is not enough for recovering the target tensor, especially when the ratio of available elements is extremely low. To address this problem, we suggest a novel low-rank tensor completion model by exploiting both low-tubal-rankness and smoothness. Especially, motivated by the capability of framelet preserving details, we characterize the spatial smoothness by framelet regularization and the smoothness of the third mode by total variation (TV) regularization. The resulting convex optimization problem is efficiently tackled by a carefully designed alternating direction method of multipliers (ADMM) algorithm. Extensive numerical results including color images, videos, and fluorescence microscope images validate the superiority of our method over the competing methods.

INDEX TERMS Low-rank tensor completion, tensor nuclear norm, framelet, total variation, alternating direction method of multipliers.

I. INTRODUCTION

Low-rank tensor completion (LRTC) is a next generation of low-rank matrix completion (LRMC), which has been a hot problem of research in many fields, such as color image inpainting [1], magnetic resonance imaging (MRI) data recovery [2], video processing [3], and hyperspectral/multispectral image (HSI/MSI) processing [4]–[8]. With the purpose of recovering a low-rank tensor from its partial observation, the core problem of LRTC is to accurately characterize the inherent low-rank structure of a tensor [9]–[11].

LRMC can exactly recover an unknown low-rank matrix from the partial observation by matrix rank minimization [12]. Mathematically, LRMC model can be generally written as

$$\begin{aligned} & \min_X \text{rank}(X) \\ & \text{s.t. } \mathcal{P}_\Omega(X) = F, \end{aligned} \quad (1)$$

where X and $F \in \mathbb{R}^{I_1 \times I_2}$ are the target and the observed matrices, respectively, Ω is the index set of the observed entries, and $\mathcal{P}_\Omega(\cdot)$ is the projection operator that keeps the entries

The associate editor coordinating the review of this manuscript and approving it for publication was Vincenzo Piuri.

of X in Ω while making others be zeros. However, the problem (1) is NP-hard. To overcome this issue, the nuclear norm of matrices has been proposed to approximate the rank of matrices [13], leading to a great success. The matrix singular value decomposition (SVD) is time-consuming, hence the nuclear norm of matrices is effective but not efficient. To enhance the time efficiency of approximating the rank of matrices, low-rank matrix factorization is proposed and used by many researchers [14], [15].

A tensor contains richer structural information compared with a matrix, which can represent more types of natural data, such as a video with multi-frames. Utilizing the low-rank prior of tensors, it is a feasible method to recover the underlying tensor by minimizing the tensor rank [16]. The LRTC model can be mathematically formulated as

$$\begin{aligned} & \min_{\mathcal{X}} \text{rank}(\mathcal{X}) \\ & \text{s.t. } \mathcal{P}_\Omega(\mathcal{X}) = \mathcal{F}, \end{aligned} \quad (2)$$

where \mathcal{X} and $\mathcal{F} \in \mathbb{R}^{I_1 \times \dots \times I_N}$ are the target and the observed tensors, respectively. In the LRTC problem, the definition of the rank of tensors is the fundamental problem, which lacks uniqueness.

The tensors in practical applications are often of low-rank, so many researchers have been devoted to defining the tensor rank lies in the corresponding tensor decompositions such as the CANDECOMP/PARAFAC (CP) [17], Tucker [18] and tensor train (TT) [19] or tensor-tensor product (t-product) [20]. The CP decomposition [21], [22] and the Tucker decomposition [23]–[25] are used commonly, the corresponding tensor ranks of which are denoted as CP-rank and Tucker-rank, respectively. However, the calculation of CP-rank is NP-hard, while the CP-rank has no relaxation which limits its application. The calculation of Tucker-rank is relatively simple, as it relies on the matrix rank. However, directly minimizing the Tucker-rank is also NP-hard. Introducing the sum of nuclear norm (SNN) as a convex relaxation of the Tucker-rank, Liu *et al.* [26] proposed an SNN-based LRTC model with three solving algorithms (SiLRTC, FaLR-TC, and HaLRTC). In addition, to solve the disadvantage of the Tucker-rank that its components are ranks of matrices constructed based on an unbalanced matricization scheme, another type of tensor rank, the TT rank, is proposed [19]. The TT rank consists of ranks of matrices formed by a well-balanced matricization scheme, i.e. matricize the tensor along permutations of modes [27], [28]. However, the unfolding operation involved in the definition of the Tucker-rank would destroy the intrinsic structure of the tensors. This implies that the Tucker-rank, SNN-based methods and the TT rank all could not preserve the intrinsic structure of the target tensors well. Recently, based on tensor-tensor product (t-product) [20], a novel tool named tensor singular value decomposition (t-SVD) and its induced tensor tubal rank and tensor multi rank have been proposed [11], [20], [29]. Moreover, being a convex surrogate for multi rank, the tensor nuclear norm (TNN) has shown its effectiveness to keep the intrinsic structure of tensors [30]–[33]. The TNN-based LRTC model can be written as

$$\begin{aligned} & \min_{\mathcal{X}} \|\mathcal{X}\|_* \\ & \text{s.t. } \mathcal{P}_{\Omega}(\mathcal{X}) = \mathcal{F}, \end{aligned} \quad (3)$$

where $\|\mathcal{X}\|_* := \sum_{i=1}^{n_3} \|\tilde{\mathcal{X}}^{(i)}\|_*$, $\tilde{\mathcal{X}}^{(i)}$ is the i -th frontal slice of $\tilde{\mathcal{X}}$, and $\tilde{\mathcal{X}} = \text{fft}(\mathcal{X}, [], 3)$, which means $\tilde{\mathcal{X}}$ is generated by performing the Discrete Fourier Transformation (DFT) along each tube of \mathcal{X} . In this paper, to avoid the tensor matricization and maintain the intrinsic data structure, we use tensor singular decomposition to exploit the global low-rank structure of tensors.

Additionally, the afore-discussed low-rankness is not enough, and the real images and videos have the property of smoothness in the spatial and third dimension. The total variation (TV) has been shown its effectiveness to promote smoothness in image processing [4], [25], [36]–[39]. Recently, Song *et al.* [40] extended classic TV to a t-product, and they designed difference tensors when multiplied by a tensor \mathcal{X} takes the gradient of \mathcal{X} . And Jiang *et al.* [35] introduced an anisotropic TV into low-rank tensor completion by considering the smoothness in the spatial domain. However,

TV usually leads to undesirable staircase effect [41]–[44]. Due to the diversity of filters and the multi-level tight frame system, framelet has recently emerged as one of the most successful regularizations for preserving details [45], [46]. Ron and Shen [47] first gave the framelets constructed from piecewise linear B-spline. Recently, Cai *et al.* [48] proposed a discrete wavelet frame based approach for image restoration, and they provided the piecewise linear framelets constructed by tensor product. In this paper, we consider framelet regularization to characterize the smoothness in the spatial domain. We suggest the following LRTC model by combining framelet regularization and TV regularization, named smooth TNN (STNN) and formulated as

$$\begin{aligned} & \min_{\mathcal{X}} \|\mathcal{X}\|_* + \lambda_1 \|W\mathcal{X}_{(3)}^T\|_{1,1} + \lambda_2 \|D_s\mathcal{X}_{(3)}\|_{1,1} \\ & \text{s.t. } \mathcal{P}_{\Omega}(\mathcal{X}) = \mathcal{F}, \end{aligned} \quad (4)$$

where λ_1 and λ_2 are regular parameters which are used to balance each term, W is the framelet transform matrix [2]. In summary, STNN has the TNN term, the framelet regularization, and the TV regularization. First, the TNN term can effectively capture the global low-rankness of underlying tensors. Second, the framelet regularization is used to exploit the smooth prior of the underlying tensor in the spatial domain, which can also preserve the details due to the diversity of filters and the multi-level tight frame system. Final, the TV regularization is introduced to exploit the smoothness along the third dimension (e.g., the temporal mode in video data). Therefore, we can reasonably get better results, on account of utilizing local smoothness and global low-rankness fully.

The recovered results for one fluorescence microscope image with the sampling rate (SR) = 20% (seen Fig. 1) show the superiority of STNN. We observe that the estimated result by STNN is visually the best among those by all compared methods. It is clear from Fig. 1 that the result outputted by TNN remains a small number of missing entries, while the TNN-3DTV method tends to smooth the image details, although TNN-3DTV can better complete the missing entries. Apparently, the method we proposed preferably preserve the details and geometric features. These observations from Fig. 1 fit well with the fore discussion of our motivation.

This paper mainly has three contributions:

- We suggest a novel LRTC model, which can simultaneously exploit the global low-rankness and the local smoothness of a tensor.
- We design an efficient ADMM algorithm to solve the LRTC model and its convergence is theoretically guaranteed.
- As demonstrated in the results of numerical experiments, the superiority of STNN is clear.

The remainder of this paper is structured as follows: Section II introduces some basic notations. Section III proposes the STNN model and gives an efficient ADMM algorithm. Section IV evaluates the performance of STNN comparing

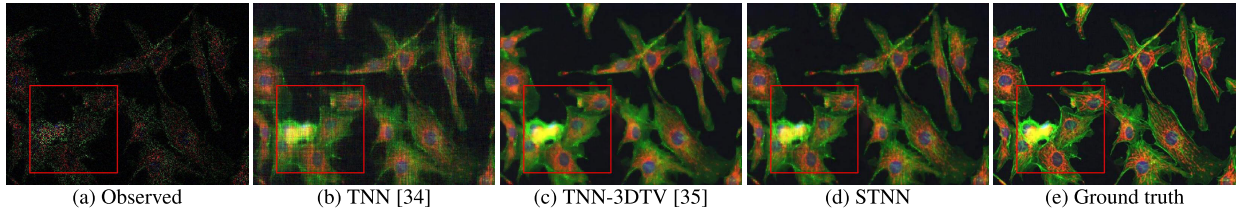


FIGURE 1. The results recovered by TNN [34], TNN-3DTV [35], and STNN with this fluorescence microscope image.

with competing methods. Section V finally shows some conclusions of this paper.

II. NOTATIONS AND PRELIMINARIES

In this section, we give some related tensor basic notations and briefly present some related definitions that will be used in this work [9], [31].

A. TENSOR BASICS

For the sake of brevity, we denote vectors, matrices, and tensors by bold lowercase letters (e.g., \mathbf{x}), the uppercase letters (e.g., X), and the calligraphic letters (e.g., \mathcal{X}), respectively. For a tensor $\mathcal{X} \in \mathbb{R}^{n_1 \times n_2 \times n_3}$, we denote its (i, j, s) -th element as $\mathcal{X}(i, j, s)$ or \mathcal{X}_{ijs} , its (i, j) -th mode-1, mode-2, and mode-3 fibers as $\mathcal{X}(:, i, j)$, $\mathcal{X}(i, :, j)$, and $\mathcal{X}(i, j, :)$, respectively. Moreover, we denote the i -th horizontal, lateral, and frontal slices of \mathcal{X} as $\mathcal{X}(i, :, :)$, $\mathcal{X}(:, i, :)$, and $\mathcal{X}(:, :, i)$ respectively.

The Frobenius norm of \mathcal{X} is defined as

$$\|\mathcal{X}\|_F := \left(\sum_{i,j,s} |\mathcal{X}(i, j, s)|^2 \right)^{\frac{1}{2}}.$$

We define the inner product of two tensors \mathcal{X} and \mathcal{Y} as follow:

$$\langle \mathcal{X}, \mathcal{Y} \rangle = \sum_{i,j,s} x_{ijs} \cdot y_{ijs},$$

For a tensor $\mathcal{X} \in \mathbb{R}^{n_1 \times n_2 \times n_3}$, the block circulation operation [49] is defined as

$$\text{bcirc}(\mathcal{X}) := \begin{pmatrix} X^{(1)} & X^{(n_3)} & \dots & X^{(2)} \\ X^{(2)} & X^{(1)} & \dots & X^{(3)} \\ \vdots & \vdots & \ddots & \vdots \\ X^{(n_3)} & X^{(n_3-1)} & \dots & X^{(1)} \end{pmatrix} \in \mathbb{R}^{n_1 n_3 \times n_2 n_3}.$$

The block diagonalization operation and its inverse operation are defined as

$$\text{bdiag}(\mathcal{X}) := \begin{pmatrix} X^{(1)} & & & \\ & X^{(2)} & & \\ & & \ddots & \\ & & & X^{(n_3)} \end{pmatrix} \in \mathbb{R}^{n_1 n_3 \times n_2 n_3},$$

$$\text{bdfold}(\text{bdiag}(\mathcal{X})) := \mathcal{X}.$$

We also define the following operator

$$\text{unfold}(\mathcal{X}) = \begin{bmatrix} X^{(1)} \\ X^{(2)} \\ \vdots \\ X^{(n_3)} \end{bmatrix}, \text{fold}(\text{unfold}(\mathcal{X})) = \mathcal{X}.$$

Definition 1 (t-Product [20]): Let $\mathcal{X} \in \mathbb{R}^{n_1 \times n_2 \times n_3}$ and $\mathcal{Y} \in \mathbb{R}^{n_2 \times l \times n_3}$. Then the t-product $\mathcal{X} * \mathcal{Y}$ is a tensor of size $n_1 \times l \times n_3$,

$$\mathcal{X} * \mathcal{Y} = \text{fold}(\text{bcirc}(\mathcal{X}) \cdot \text{unfold}(\mathcal{Y})).$$

Definition 2 (Special Tensors [20]): The identity tensor $\mathcal{I} \in \mathbb{R}^{n_1 \times n_2 \times n_3}$ is the tensor whose first frontal slice is the identity matrix, and other frontal slices are all zeros. The conjugate transpose of a tensor $\mathcal{X} \in \mathbb{R}^{n_1 \times n_2 \times n_3}$, denote as \mathcal{X}^T , is the tensor obtained by conjugate transposing each of the frontal slices and then reversing the order of transposed frontal slices 2 through n_3 . A tensor $\mathcal{Q} \in \mathbb{R}^{n_1 \times n_2 \times n_3}$ is orthogonal, which means the tensor satisfies $\mathcal{Q} * \mathcal{Q}^T = \mathcal{Q}^T * \mathcal{Q} = \mathcal{I}$.

Theorem 1 (t-SVD [20]): For a tensor $\mathcal{X} \in \mathbb{R}^{n_1 \times n_2 \times n_3}$, it can be factored as $\mathcal{X} = \mathcal{U} * \mathcal{S} * \mathcal{V}^T$, where $\mathcal{U} \in \mathbb{R}^{n_1 \times n_1 \times n_3}$ and $\mathcal{V} \in \mathbb{R}^{n_2 \times n_2 \times n_3}$ are the orthogonal tensors, and $\mathcal{S} \in \mathbb{R}^{n_1 \times n_2 \times n_3}$ is a f-diagonal tensor whose each frontal slices is a diagonal matrix. The t-SVD can be efficiently obtained by computing a series of matrix SVDs in the Fourier domain.

Definition 3 (Tensor Tubal Rank and Multi Rank [30]): For a tensor $\mathcal{X} \in \mathbb{R}^{n_1 \times n_2 \times n_3}$, the tensor multi rank of \mathcal{X} is a vector $\text{rank}_m(\mathcal{X}) \in \mathbb{R}^{n_3}$, whose i -th element is the rank of i -th frontal slice of \mathcal{X} , where $\bar{\mathcal{X}}$ is the Discrete Fourier Transform (DFT) of $\mathcal{X} \in \mathbb{R}^{n_1 \times n_2 \times n_3}$ along each tube, i.e., $\bar{\mathcal{X}} = \text{fft}(\mathcal{X}, [], 3)$. The tubal rank of \mathcal{X} , denote as $\text{rank}_t(\mathcal{X})$, is defined as the number of non-zero tubes of \mathcal{S} . The relationship between these two ranks is $\text{rank}_t(\mathcal{X}) = \max(\text{rank}_m(\mathcal{X}))$.

Definition 4 (TNN) [30]: The tensor nuclear norm (TNN) of a tensor $\mathcal{X} \in \mathbb{R}^{n_1 \times n_2 \times n_3}$, denoted as $\|\mathcal{X}\|_*$, is defined as the sum of singular values of all the frontal slices of $\bar{\mathcal{X}}$, i.e.,

$$\|\mathcal{X}\|_* := \sum_{i=1}^{n_3} \|\bar{X}^{(i)}\|_*,$$

where $\bar{X}^{(i)}$ is the i -th frontal slice of $\bar{\mathcal{X}}$.

III. THE PROPOSED MODEL AND ALGORITHM

In this section, by applying TNN, framelet, and TV to the LRTC problem, we propose an LRTC model and develop an ADMM-based algorithm to address it.

A. THE PROPOSED MODEL

The goal of tensor completion is estimating the missing elements from an incomplete observation tensor. Considering a tensor $\mathcal{X} \in \mathbb{R}^{n_1 \times n_2 \times n_3}$, the proposed STNN-based LRTC model is formulated as

$$\min_{\mathcal{X}} \|\mathcal{X}\|_* + \lambda_1 \|WX_{(3)}^T\|_{1,1} + \lambda_2 \|D_s X_{(3)}\|_{1,1} + \iota(\mathcal{X})$$

where λ_1 and λ_2 are regularization parameters, \mathcal{X} and \mathcal{F} are the target and the observed tensors, respectively, and $\iota(\cdot)$ is the indicator function as follow:

$$\iota(\mathcal{X}) := \begin{cases} 0, & \text{if } \mathcal{P}_\Omega(\mathcal{X}) = \mathcal{F}, \\ \infty, & \text{otherwise.} \end{cases}$$

There are three important parts of STNN. The first term is the TNN term, which is used to catch the global low-rankness. Hence the reason for introducing this term is TNN can well characterize the global structural information of a tensor. The second term is the framelet regularization term $\|WX_{(3)}^T\|_{1,1}$, where W indicates the framelet transform matrix satisfying $W^T W = I$, and $X_{(3)}$ denotes the mode-3 unfolding of \mathcal{X} [45]. Mathematically,

$$X_{(3)}^T = [\mathbf{x}_{31}, \mathbf{x}_{32}, \dots, \mathbf{x}_{3i}, \dots, \mathbf{x}_{3n_3}] \in \mathbb{R}^{n_3 \times n_1 n_2},$$

where $\mathbf{x}_{3i} \in \mathbb{R}^{n_1 n_2}$ ($i = 1, \dots, n_3$) is the i -th vectorized factor image. Notably, this framelet regularization term can be used to preserve abundant details in spatial domain. The last term is the TV regularization which can boost the smoothness along the third mode of the target tensor \mathcal{X} , i.e., $\|D_s X_{(3)}\|_{1,1}$, where D_s is an $n_3 \times n_3$ difference matrix

$$D_s = \begin{pmatrix} -1 & 1 & \dots & 0 & 0 \\ 0 & -1 & \dots & 0 & 0 \\ \vdots & \vdots & \ddots & \vdots & \vdots \\ 0 & 0 & \dots & -1 & 1 \\ 1 & 0 & \dots & 0 & -1 \end{pmatrix}.$$

In a brief summary, STNN takes advantage of both the global low-rankness and the local smoothness among the spatial and third dimensions. As demonstrated in our numerical experiments, TNN term, framelet regularization, and TV regularization would be effective to boost these two priors.

B. THE PROPOSED ALGORITHM

Many solvers are available for the proposed convex model [50]. Here we design an efficient algorithm based on ADMM for tackling the optimization problem. This model can be equivalently reformulated as a constrained problem as follows:

$$\begin{aligned} & \min_{\mathcal{X}, \mathcal{Y}, Z, Q, \mathcal{V}} \|\mathcal{Y}\|_* + \lambda_1 \|Z\|_{1,1} + \lambda_2 \|Q\|_{1,1} + \iota(\mathcal{V}) \\ & \text{s.t. } \mathcal{Y} = \mathcal{X}, \\ & \quad Z = WX_{(3)}^T, \\ & \quad Q = D_s X_{(3)}, \\ & \quad \mathcal{V} = \mathcal{X}, \end{aligned} \tag{5}$$

where $\mathcal{Y} \in \mathbb{R}^{n_1 \times n_2 \times n_3}$, $Z \in \mathbb{R}^{n_1 n_2 \times n_3}$, $Q \in \mathbb{R}^{n_3 \times n_1 n_2}$, and $\mathcal{V} \in \mathbb{R}^{n_1 \times n_2 \times n_3}$. The optimization problem is well-structured, since two blocks of variables are separated. Therefore, the problem fits the framework of ADMM, while the convergence of the algorithm is theoretically guaranteed. Then the augmented Lagrangian function of (5) is

$$\begin{aligned} L(\mathcal{X}, \mathcal{Y}, Z, Q, \mathcal{V}) &= \|\mathcal{Y}\|_* + \langle \mathcal{X} - \mathcal{Y}, \mathcal{M} \rangle + \frac{\beta_1}{2} \|\mathcal{X} - \mathcal{Y}\|_F^2 \\ &\quad + \lambda_1 \|Z\|_{1,1} + \langle WX_{(3)}^T - Z, \Lambda \rangle + \frac{\beta_2}{2} \|WX_{(3)}^T - Z\|_F^2 \\ &\quad + \lambda_2 \|Q\|_{1,1} + \langle D_s X_{(3)} - Q, \Phi \rangle + \frac{\beta_3}{2} \|D_s X_{(3)} - Q\|_F^2 \\ &\quad + \iota(\mathcal{V}) + \langle \mathcal{X} - \mathcal{V}, \mathcal{N} \rangle + \frac{\beta_4}{2} \|\mathcal{X} - \mathcal{V}\|_F^2, \end{aligned}$$

where \mathcal{M} , \mathcal{N} , Λ , and Φ are the Lagrange multipliers, β_1 , β_2 , β_3 , and β_4 are the penalty parameters. Then two easier and smaller subproblems can replace the joint minimization problem, i.e., solving these two blocks $[\mathcal{Y}, Z, Q, \mathcal{V}]$ and \mathcal{X} in an alternating order. Finally, update the Lagrangian multipliers $[\mathcal{M}, \Lambda, \Phi, \mathcal{N}]$.

In Step 1, we solve the $[\mathcal{Y}, Z, Q, \mathcal{V}]$ subproblem. Since the variables \mathcal{Y} , Z , Q , and \mathcal{V} are decoupled, their optimal solutions can be calculated separately as follow:

$$\mathcal{Y}^{k+1} = \arg \min_{\mathcal{Y}} \|\mathcal{Y}\|_* + \frac{\beta_1}{2} \|\mathcal{X} - \mathcal{Y} + \frac{\mathcal{M}}{\beta_1}\|_F^2,$$

which exhibits a closed-form solution

$$\mathcal{Y}^{k+1} = \mathcal{D}_{\frac{1}{\beta_1}}(\mathcal{X} + \frac{\mathcal{M}}{\beta_1}), \tag{6}$$

via the following Theorem 1.

Theorem 1 (t-SVT) [31]: Assuming that $\mathcal{T} \in \mathbb{R}^{n_1 \times n_2 \times n_3}$ is a three-way tensor, an explicit solution of

$$\arg \min_{\mathcal{Y}} \tau \|\mathcal{Y}\|_* + \frac{\beta_1}{2} \|\mathcal{Y} - \mathcal{T}\|_F^2,$$

is given by the tensor singular value thresholding (t-SVT)

$$\mathcal{Y} = \mathcal{D}_\tau(\mathcal{T}) := \mathcal{U} * \mathcal{S}_\tau * \mathcal{V}^T,$$

where $\mathcal{T} = \mathcal{U} * \mathcal{S} * \mathcal{V}^T$ and \mathcal{S}_τ is an $n_1 \times n_2 \times n_3$ tensor which satisfies

$$\bar{\mathcal{S}}_\tau(i, i, k) = \max (\bar{\mathcal{S}}(i, i, k) - \tau, 0),$$

where $\bar{\mathcal{S}} = \text{fft}(\mathcal{S}, [], 3)$ and τ is a threshold. The complexity of computing \mathcal{Y} is $O(n_3 \min(n_1^2 n_2, n_1 n_2^2) + n_1 n_2 n_3 \log(n_3))$. The Z -subproblem is

$$Z^{k+1} = \arg \min_Z \lambda_1 \|Z\|_{1,1} + \frac{\beta_2}{2} \|WX_{(3)}^T - Z + \frac{\Lambda}{\beta_2}\|_F^2,$$

which possesses an explicit solution

$$Z^{k+1} = \mathcal{S}_{\frac{\lambda_1}{\beta_2}}(WX_{(3)}^{k+1} + \frac{\Lambda}{\beta_2}). \tag{7}$$

Here $S_\tau(\cdot)$ is the element-wise soft-thresholding operator:

$$S_\tau(x) = \begin{cases} 0, & \text{if } |x| \leq \tau, \\ \text{sign}(x)(|x| - \tau), & \text{if } |x| > \tau. \end{cases}$$

The cost of computing $WX_{(3)}^T$ is $O(lm^2 n_1 n_2 n_3)$, where l is the level of the framelet and m is the number of filters, so the cost of computing Z is $O(lm^2 n_1 n_2 n_3)$. Then the Q -subproblem is

$$Q^{k+1} = \arg \min_Q \lambda_2 \|Q\|_{1,1} + \frac{\beta_3}{2} \|D_s X_{(3)} - Q + \frac{\Phi}{\beta_3}\|_F^2,$$

which can be calculated by

$$Q^{k+1} = S_{\frac{\lambda_2}{\beta_3}}(D_s X_{(3)}^k + \frac{\Phi^k}{\beta_3}). \quad (8)$$

The cost of computing Q is $O(n_1 n_2 n_3^2)$. The \mathcal{V} -subproblem is

$$\mathcal{V}^{k+1} = \arg \min_{\mathcal{V}} \iota(\mathcal{V}) + \frac{\beta_4}{2} \|\mathcal{X} - \mathcal{V} + \frac{\mathcal{N}}{\beta_4}\|_F^2,$$

which has an explicit solution

$$\mathcal{V}^{k+1} = \mathcal{P}_{\Omega^c}(\mathcal{X}^k + \frac{\mathcal{N}^k}{\beta_4}) + \mathcal{F}, \quad (9)$$

where Ω^C is the complementary set of Ω . The cost of computing \mathcal{V} is $O(n_1 n_2 n_3)$.

In Step 2, the \mathcal{X} -subproblem is

$$\begin{aligned} \mathcal{X}^{k+1} = & \arg \min_{\mathcal{X}} \frac{\beta_1}{2} \|\mathcal{X} - \mathcal{Y} + \frac{\mathcal{M}}{\beta_1}\|_F^2 \\ & + \frac{\beta_2}{2} \|WX_{(3)}^T - Z + \frac{\Lambda}{\beta_2}\|_F^2 \\ & + \frac{\beta_3}{2} \|D_s X_{(3)} - Q + \frac{\Phi}{\beta_3}\|_F^2 \\ & + \frac{\beta_4}{2} \|\mathcal{X} - \mathcal{V} + \frac{\mathcal{N}}{\beta_4}\|_F^2. \end{aligned} \quad (10)$$

Since $\|\mathcal{X}\|_F^2 = \|X_{(3)}\|_F^2$ and $\|X\|_F^2 = \|X^T\|_F^2$, the problem (10) can be rewritten as

$$\begin{aligned} \arg \min_{X_{(3)}} & \frac{\beta_1}{2} \|X_{(3)} - Y_{(3)} + \frac{M_{(3)}}{\beta_1}\|_F^2 \\ & + \frac{\beta_2}{2} \|(WX_{(3)}^T - Z + \frac{\Lambda}{\beta_2})^T\|_F^2 \\ & + \frac{\beta_3}{2} \|D_s X_{(3)} - Q + \frac{\Phi}{\beta_3}\|_F^2 \\ & + \frac{\beta_4}{2} \|X_{(3)} - V_{(3)} + \frac{N_{(3)}}{\beta_4}\|_F^2. \end{aligned}$$

The normal equation of the problem (10) is a classical Sylvester matrix equation as

$$\begin{aligned} & (\beta_1 I + \beta_3 D_s^T D_s + \beta_4 I) X_{(3)} + \beta_2 X_{(3)} W^T W \\ & = \beta_1 Y_{(3)} - M_{(3)} + \beta_2 [W^T (Z - \frac{\Lambda}{\beta_2})]^T \\ & + \beta_3 D_s^T (Q - \frac{\Phi}{\beta_3}) + \beta_4 V_{(3)} - N_{(3)}. \end{aligned}$$

Noting $W^T W = I$, the problem (10) possesses an explicit solution

$$\begin{aligned} X_{(3)} = & F^* \Psi^{-1} F (\beta_1 Y_{(3)} - M_{(3)} + \beta_2 [W^T (Z - \frac{N}{\beta_2})]^T \\ & + \beta_3 D_s^T (Q - \frac{\Phi}{\beta_3}) + \beta_4 V_{(3)} - N_{(3)}), \end{aligned} \quad (11)$$

where $\beta_1 I + \beta_2 I + \beta_3 D_s^T D_s + \beta_4 I = F^* \Psi F$, Ψ is a diagonal matrix, F and F^* are the discrete transform matrix and its inverse transform matrix. The cost of computing \mathcal{X} is $O(n_3^3 + lm^2 n_1 n_2 n_3 + n_3^2 \log(n_3))$.

In Step 3, the Lagrange multipliers \mathcal{M} , Λ , Φ , and \mathcal{N} can be updated as

$$\begin{aligned} \mathcal{M}^{k+1} &= \mathcal{M}^k + \beta_1 (\mathcal{X}^{k+1} - \mathcal{Y}^{k+1}), \\ \Lambda^{k+1} &= \Lambda^k + \beta_2 (W(X_{(3)}^{k+1})^T - Z^{k+1}), \\ \Phi^{k+1} &= \Phi^k + \beta_3 (D_s X_{(3)}^{k+1} - Q^{k+1}), \\ \mathcal{N}^{k+1} &= \mathcal{N}^k + \beta_4 (\mathcal{X}^{k+1} - \mathcal{V}^{k+1}). \end{aligned} \quad (12)$$

The proposed ADMM algorithm can then be organized as Algorithm 1.

Algorithm 1 The Proposed ADMM Algorithm for Solving (5)

Input: The observed tensor \mathcal{F} , index set Ω , parameters β_1 , β_2 , β_3 , β_4 , λ_1 , and λ_2 .

Initialization: \mathcal{X}_0 , \mathcal{Y}_0 , Z_0 , Q_0 , \mathcal{V}_0 , \mathcal{M}_0 , Λ_0 , Φ_0 , and \mathcal{N}_0 initialized to 0, $k = 0$, $k_{\max} = 150$.

while not converged and $k < k_{\max}$ **do**
 Update $\mathcal{Y}^{(k+1)}$ via (6);
 Update $Z^{(k+1)}$ via (7);
 Update $Q^{(k+1)}$ via (8);
 Update $\mathcal{V}^{(k+1)}$ via (9);
 Update $\mathcal{X}^{(k+1)}$ via (11);
 Update $\mathcal{M}^{(k+1)}$, $\Lambda^{(k+1)}$, $\Phi^{(k+1)}$, and $\mathcal{N}^{(k+1)}$ via (12);
end while

Output: The completed tensor \mathcal{X} .

Finally, we see that every step of Algorithm 1 has an explicit solution. Thus, the proposed ADMM algorithm is efficiently implementable. The complexity of computing all variables \mathcal{Y} , Z , Q , and \mathcal{X} at each iteration is $O(n_3 \min(n_1^2 n_2, n_1 n_2^2) + lm^2 n_1 n_2 n_3 + n_1 n_2 n_3^2 + n_3^3)$.

IV. NUMERICAL EXPERIMENTS

In this section, we conduct the performance evaluation and analysis of the STNN method, basing the results in three sets of experiments: color image completion, fluorescence microscope image completion, and gray video completion. We compare STNN with two related methods: TNN [34] and TNN-3DTV [35]. To measure the quality of the recovered results, we employ the peak signal to noise rate (PSNR) and the structural similarity index (SSIM) [51] as the quality metrics. Higher values in quality metrics indicate better performance of recovery. The relative change (RelCha) is

TABLE 1. The quality metrics values of three completion methods on 11 color images.

Images	SR	PSNR			SSIM		
		TNN	TNN-3DTV	STNN	TNN	TNN-3DTV	STNN
 256 × 256 × 3	20%	22.419	25.591	25.856	0.7888	0.9069	0.9371
	30%	25.662	27.817	28.411	0.8719	0.9380	0.9424
	40%	28.082	29.148	30.289	0.9175	0.9564	0.9737
 512 × 512 × 3	20%	23.144	26.039	26.867	0.8534	0.8765	0.9004
	30%	25.788	28.261	29.264	0.9003	0.9118	0.9382
	40%	27.886	30.311	31.001	0.9532	0.9481	0.9941
 512 × 512 × 3	20%	25.519	27.055	27.836	0.8242	0.9221	0.9346
	30%	27.998	29.732	30.638	0.9014	0.9531	0.9668
	40%	30.401	31.779	32.771	0.9429	0.9708	0.9799
 512 × 512 × 3	20%	24.666	27.037	27.763	0.7510	0.9122	0.9319
	30%	27.488	29.706	30.613	0.8541	0.9434	0.9681
	40%	29.889	31.733	32.813	0.9149	0.9627	0.9807
 586 × 695 × 3	20%	28.248	28.845	29.746	0.8734	0.8665	0.9001
	30%	30.889	31.482	32.141	0.9323	0.9118	0.9328
	40%	33.614	34.007	34.625	0.9632	0.9401	0.9812
 321 × 481 × 3	20%	22.348	23.774	24.653	0.5052	0.7519	0.7718
	30%	24.981	26.957	27.291	0.6685	0.8217	0.8861
	40%	27.737	29.645	29.678	0.7898	0.8721	0.9305
 512 × 768 × 3	20%	21.864	23.271	24.053	0.6052	0.7437	0.7941
	30%	24.173	25.831	26.171	0.7695	0.8637	0.8897
	40%	26.838	28.537	28.602	0.7888	0.8772	0.9296
 512 × 768 × 3	20%	22.929	25.753	26.041	0.6923	0.8945	0.8993
	30%	25.863	28.583	29.263	0.8988	0.9289	0.9612
	40%	28.903	30.984	31.899	0.9322	0.9571	0.9901
 512 × 768 × 3	20%	21.641	25.912	26.061	0.8909	0.9439	0.9764
	30%	24.961	28.437	29.411	0.9599	0.9731	0.9902
	40%	28.088	30.776	32.174	0.9766	0.9842	0.9982
 768 × 1024 × 3	20%	26.473	28.792	29.253	0.8923	0.9466	0.9755
	30%	29.346	30.835	32.179	0.9502	0.9709	0.9890
	40%	32.024	33.252	34.485	0.9755	0.9836	0.9973
 768 × 1024 × 3	20%	23.373	24.295	24.354	0.6685	0.8822	0.8857
	30%	25.761	25.682	26.104	0.8922	0.9302	0.9531
	40%	27.906	27.057	27.996	0.9382	0.9572	0.9818
Average	20%	23.875	25.988	26.589	0.7587	0.8770	0.9006
	30%	26.628	28.484	29.226	0.8726	0.9224	0.9471
	40%	29.215	30.657	31.485	0.9175	0.9463	0.9761

adopted as the stopping criterion of all methods, which is defined as

$$\text{RelCha} = \frac{\|\mathcal{X}^{l+1} - \mathcal{X}^l\|_F}{\|\mathcal{X}^l\|_F}.$$

In all experiments, when RelCha is smaller than the tolerance 10^{-3} , we stop the iterations.

In all experiments, parameters of two compared methods TNN [34] and TNN-3DTV [35] are set based on authors' codes or suggestions in their papers. For STNN, the parameters in the framelet transform are set as: the filter parameter frame = 3, the level parameters Level are selected from {1, 2} and WLevel = 0.3. Besides, the regularization

parameters $\{\lambda_1, \lambda_2\}$ and the penalty parameters $\{\beta_1, \beta_2, \beta_3, \beta_4\}$ are selected from a candidate set: $\{10^{-4}, 10^{-3}, 10^{-2}, 10^{-1}, 1, 10^1, 10^2, 10^3, 10^4\}$ in our experiments. In all experiments, the methodology for sampling the data is purely random sampling.

A. COLOR IMAGE COMPLETION

In this section, eleven color images are used for the experiment. For color image completion, the sampling rates (SRs) are set to 20%, 30%, and 40%. For each SR, the quality metrics values for each completion method on 11 color images are listed in Tab. 1, and the best results are denoted in bold. From Tab. 1, it can be observed that STNN achieves the

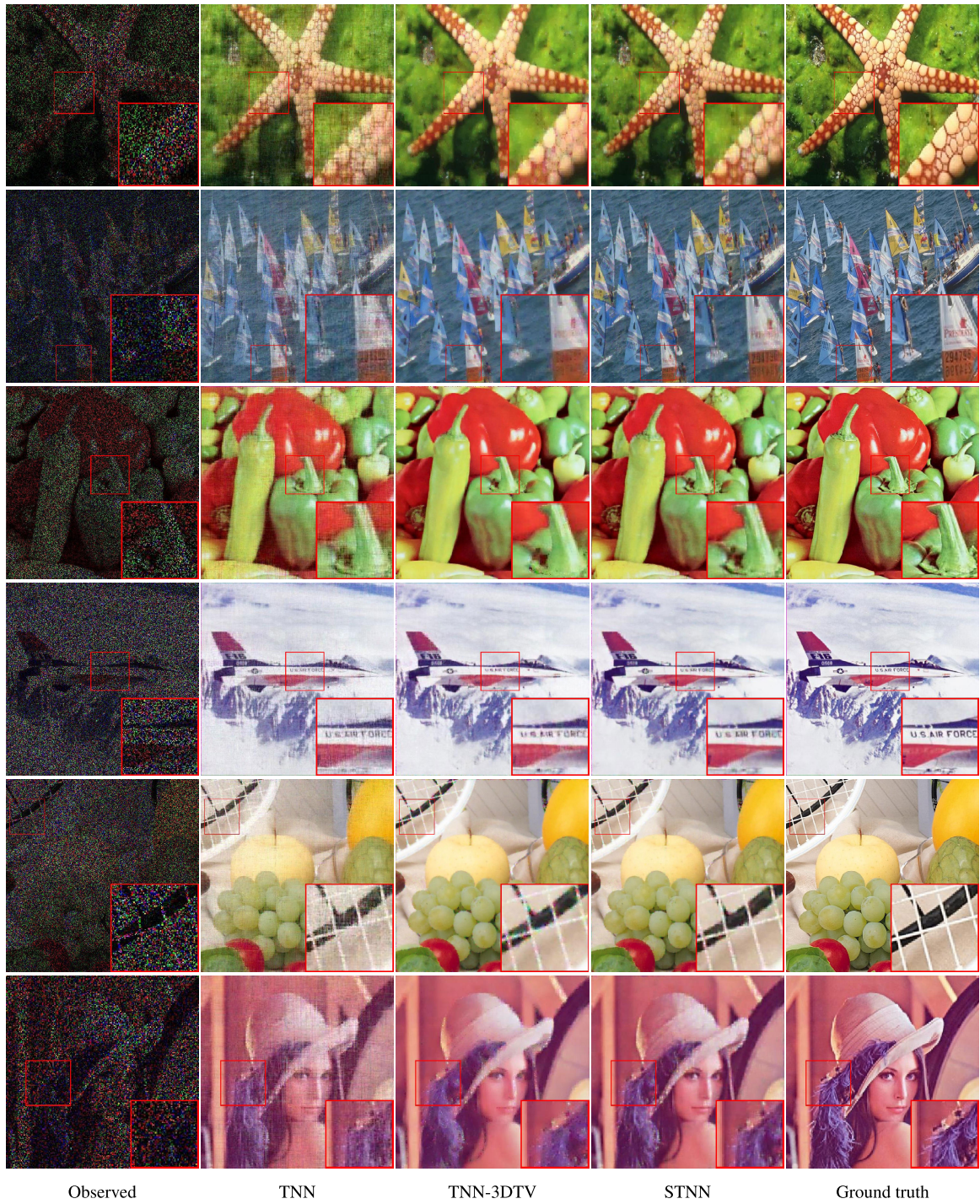


FIGURE 2. The results recovered by TNN, TNN-3DTV, and STNN on six color images with SR = 20%.

highest quality metrics values and performs obviously better than competing methods.

Fig. 2 shows the results recovered by TNN, TNN-3DTV, and STNN with six test color images. Obviously, we can see that STNN performs better than the comparison methods, which validates the characteristics of STNN. For the sake of comparison, we magnify a significant region for each of the resulting images. Compared with other methods, the

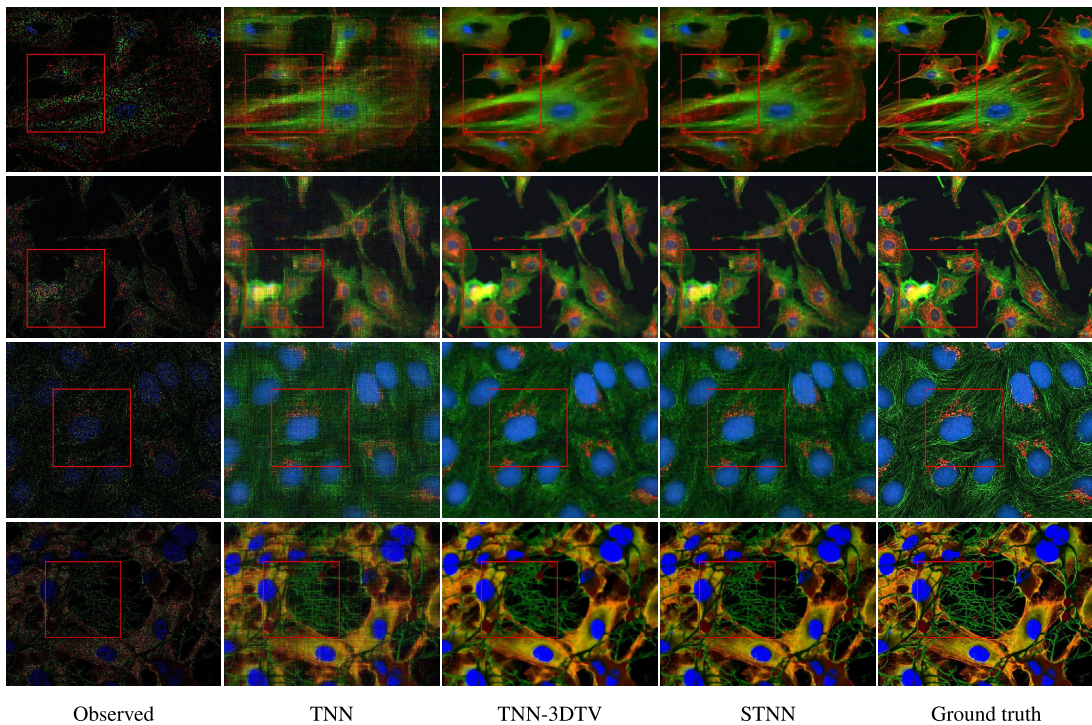
magnified image region can show that STNN provides clear and sharp spatial details, while the results obtained by TNN [34] and TNN-3DTV [35] still contain evident blurry areas.

B. FLUORESCENCE MICROSCOPE IMAGE COMPLETION

In this section, we investigate the experimental results of four fluorescence microscope images by different methods.

TABLE 2. The quality metrics values of three completion methods on fluorescence microscope images.

FMI	SR	PSNR			SSIM		
		TNN	TNN-3DTV	STNN	TNN	TNN-3DTV	STNN
	20%	21.958	25.378	25.586	0.3922	0.6614	0.6908
	30%	24.185	27.101	27.532	0.5258	0.7438	0.7895
	40%	26.325	28.497	29.507	0.6518	0.8098	0.8557
	20%	23.364	26.157	26.291	0.6752	0.8293	0.8607
	30%	25.713	27.814	28.842	0.7959	0.8896	0.9236
	40%	28.155	29.402	31.197	0.8794	0.9304	0.9577
	20%	19.146	20.787	21.586	0.5123	0.5542	0.5788
	30%	20.891	21.833	22.371	0.6651	0.6526	0.7126
	40%	22.602	22.774	23.701	0.7802	0.7424	0.8067
	20%	18.841	23.269	23.511	0.5120	0.7395	0.7836
	30%	22.049	25.105	26.423	0.6899	0.8272	0.8818
	40%	24.827	26.735	28.977	0.8130	0.8872	0.9345
Average	20%	20.827	23.890	24.192	0.5229	0.6961	0.7285
	30%	23.210	25.463	26.292	0.6692	0.7783	0.8269
	40%	25.477	26.852	28.346	0.7811	0.8425	0.8887

**FIGURE 3.** The results recovered by TNN, TNN-3DTV, and STNN on fluorescence microscope images with SR = 20%.

Fluorescence microscope images have rich details, which can highlight the advantage of framelet regularization in STNN. With the SRs: 20%, 30%, and 40%, we test fluorescence microscope image completion for each image. We reported the quality metrics values of the 4 fluorescence microscope images, and compare the results quantitatively and visually. For each SR, the quality metrics values for each completion method on 4 fluorescence microscope images are listed in Tab. 2, and the best results are denoted in bold. From Tab. 2,

it can be observed that STNN performs evidently better than competing methods.

Fig. 3 shows the results recovered by TNN, TNN-3DTV, and STNN with four fluorescence microscope images for SR = 20%. To highlight the difference of the visual results by three LRTC methods, we have framed an obvious region of recovered images. Obviously, we can see that STNN shows its visual superiority over the comparative methods. In Fig. 3, the recovered fluorescence microscope images by TNN [34]

TABLE 3. The PSNR, SSIM, and SAM values of three completion methods on gray videos.

Video	SR	PSNR			SSIM			SAM		
		TNN	TNN-3DTV	STNN	TNN	TNN-3DTV	STNN	TNN	TNN-3DTV	STNN
Containier	10%	29.857	30.218	31.595	0.9062	0.9278	0.9495	0.0306	0.0261	0.0230
	20%	34.281	34.908	36.726	0.9573	0.9637	0.9758	0.0224	0.0188	0.0164
	30%	37.587	39.312	40.221	0.9755	0.9825	0.9845	0.0172	0.0138	0.0125
	40%	40.148	41.875	43.091	0.9842	0.9842	0.9911	0.0139	0.0117	0.0101
	50%	42.921	44.316	45.865	0.9896	0.9913	0.9939	0.0113	0.0101	0.0083
Suzie	10%	28.861	29.261	30.875	0.8091	0.8606	0.8904	0.0576	0.0501	0.0479
	20%	31.713	32.061	33.247	0.8804	0.9141	0.9272	0.0454	0.0398	0.0372
	30%	33.437	34.188	36.247	0.9171	0.9361	0.9588	0.0362	0.0327	0.0269
	40%	35.941	36.373	38.289	0.9461	0.9543	0.9705	0.0294	0.0264	0.0202
	50%	37.945	38.501	39.341	0.9637	0.9675	0.9756	0.0263	0.0235	0.0193
Hall	10%	32.238	32.537	33.123	0.9384	0.9467	0.9577	0.0257	0.0238	0.0224
	20%	36.304	36.417	37.447	0.9686	0.9736	0.9761	0.0198	0.0194	0.0182
	30%	38.569	38.776	39.747	0.9789	0.9809	0.9855	0.0166	0.0154	0.0147
	40%	40.784	40.845	41.717	0.9854	0.9861	0.9895	0.0138	0.0132	0.0125
	50%	42.355	42.404	43.547	0.9895	0.9901	0.9923	0.0127	0.0121	0.0102
News	10%	30.501	30.875	30.962	0.9102	0.9272	0.9369	0.0535	0.0465	0.0452
	20%	34.182	34.765	34.784	0.9554	0.9701	0.9714	0.0389	0.0324	0.0305
	30%	36.555	37.311	37.499	0.9731	0.9807	0.9828	0.0306	0.0270	0.0244
	40%	38.718	39.187	39.617	0.9824	0.9862	0.9886	0.0252	0.0230	0.0188
	50%	40.861	40.897	41.521	0.9886	0.9903	0.9928	0.0191	0.0193	0.0162
Salesman	10%	30.453	31.166	32.185	0.9364	0.9503	0.9624	0.0351	0.0298	0.0286
	20%	34.338	35.325	35.777	0.9738	0.9799	0.9816	0.0253	0.0218	0.0210
	30%	37.021	37.592	38.292	0.9851	0.9872	0.9888	0.0203	0.0184	0.0175
	40%	39.045	39.446	40.493	0.9902	0.9912	0.9928	0.0166	0.0158	0.0146
	50%	41.264	41.486	42.339	0.9939	0.9941	0.9950	0.0137	0.0133	0.0123
Foreman	10%	23.686	24.106	24.739	0.5993	0.7701	0.7760	0.0905	0.0736	0.0702
	20%	26.527	27.194	28.136	0.7372	0.8716	0.8877	0.0681	0.0555	0.0489
	30%	28.805	29.880	30.633	0.8189	0.8948	0.9154	0.0542	0.0458	0.0401
	40%	30.956	32.067	32.920	0.8783	0.9287	0.9443	0.0427	0.0368	0.0318
	50%	33.237	34.069	34.824	0.9203	0.9472	0.9601	0.0333	0.0298	0.0260
Average	10%	29.266	29.694	30.580	0.8499	0.8971	0.9122	0.0488	0.0417	0.0396
	20%	32.891	33.445	34.353	0.9121	0.9455	0.9533	0.0367	0.0313	0.0287
	30%	35.329	36.177	37.107	0.9414	0.9604	0.9693	0.0292	0.0255	0.0227
	40%	37.599	38.299	39.355	0.9611	0.9718	0.9795	0.0236	0.0212	0.0180
	50%	39.764	40.279	41.240	0.9743	0.9801	0.9850	0.0194	0.0180	0.0154

are still blurred and the recovered fluorescence microscope images by TNN-3DTV [35] reduce block-artifacts, but there are piecewise constant in the smooth area of images.

C. VIDEO COMPLETION

In this section, six videos: *container*, *suzie*, *hall*, *news*, *salesman*, and *foreman* are tested in these experiments. In our tests, we only use the first 30 frames of each video. The size of all testing videos is $144 \times 176 \times 30$. The SRs are set to be 10%, 20%, 30%, 40%, and 50%.

For video data, we add spectral angle mapper (SAM) to measure the spectral distortions of the recovered results. Better recovered results correspond to lower values in SAM. Tab. 3 summarizes the PSNR, SSIM, and SAM of six selected

videos recovered by three LRTC methods with different SRs, and the highest values are denoted in bold. We can observe that STNN outperforms the comparison methods in terms of PSNR, SSIM, and SAM values. According to SAM values, one conclusion which can be drawn is STNN better reduces the distortions among frames than TNN [34] and TNN-3DTV [35].

To comprehensively compare the performance of three LRTC methods, we select two recovered videos *container* and *suzie* as representation. In Fig. 4, the PSNR values of each frame recovered by three compared methods are presented, so the performance comparison can be made more straightforward. By observing all the curves in Fig. 4, we can easily draw a conclusion that STNN is superior to the compared methods in terms of PSNR values.

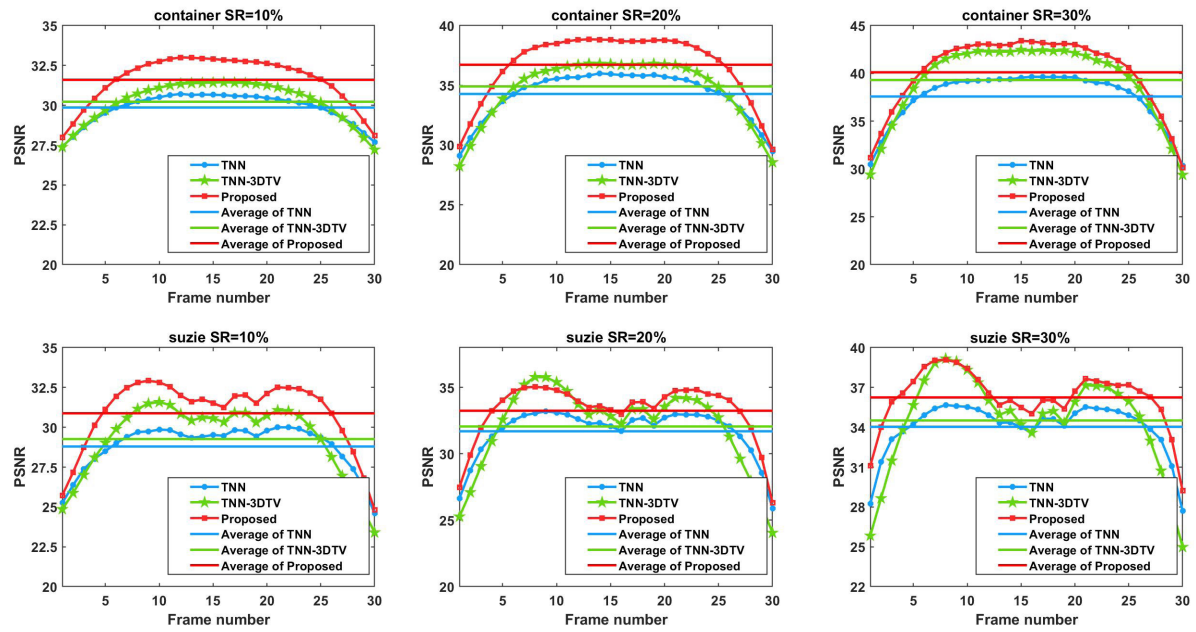


FIGURE 4. The PSNR values obtained by TNN, TNN-3DTV, and the proposed method with two completed videos.

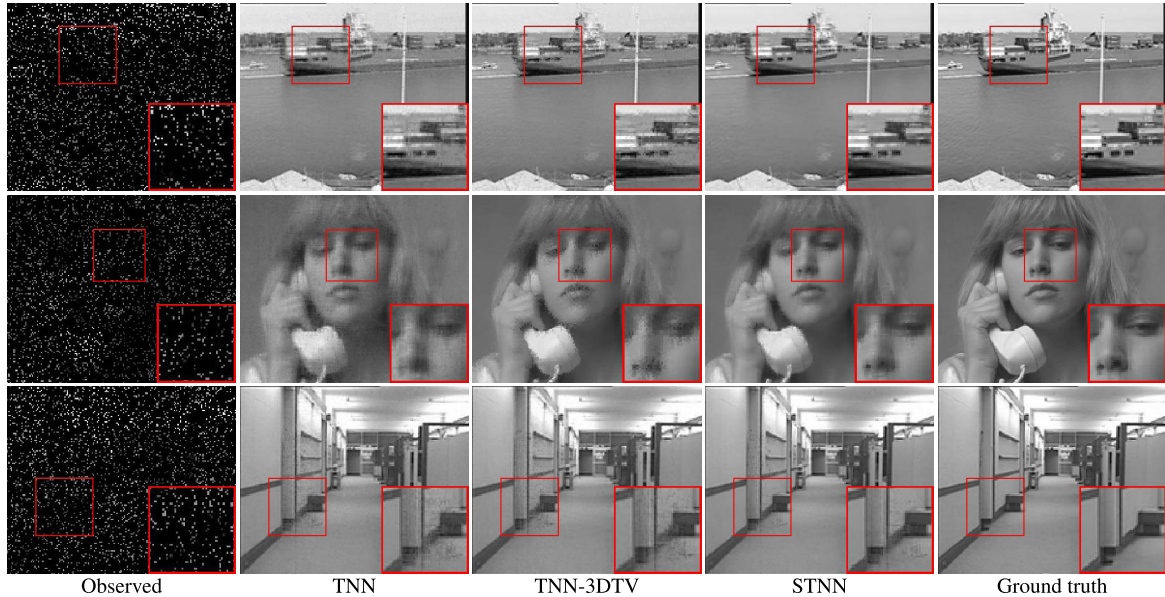


FIGURE 5. The selected frame of three videos recovered by TNN, TNN-3DTV, and STNN with SR = 10%.

Fig. 5 shows one frame located at the 15th frame in three videos which are recovered by three LRTC methods with $SR = 10\%$, which can show the visual results of videos recovered by these three methods. Besides, in order to well present the difference of the visual results by three LRTC methods, we have framed an obvious region of each recovered frame we select while magnifying the region. Apparently, the recovered videos by STNN is visually superior to those by the compared methods. Definitely, STNN has a better performance to complete the missing

entries, while finely preserving clear and sharp spatial details. For contrast methods, the results obtained by TNN [34] remain a large number of missing entries. TNN-3DTV [35] relatively outperforms TNN in missing entries completing, however, the results obtained by TNN-3DTV still contain the blurry areas. In addition, TNN-3DTV leads to some details missing.

Fig. 6 shows the pixel value of a selected tube of two videos *container* and *suzie* recovered by three compared methods with different SRs. We can observe that the curve

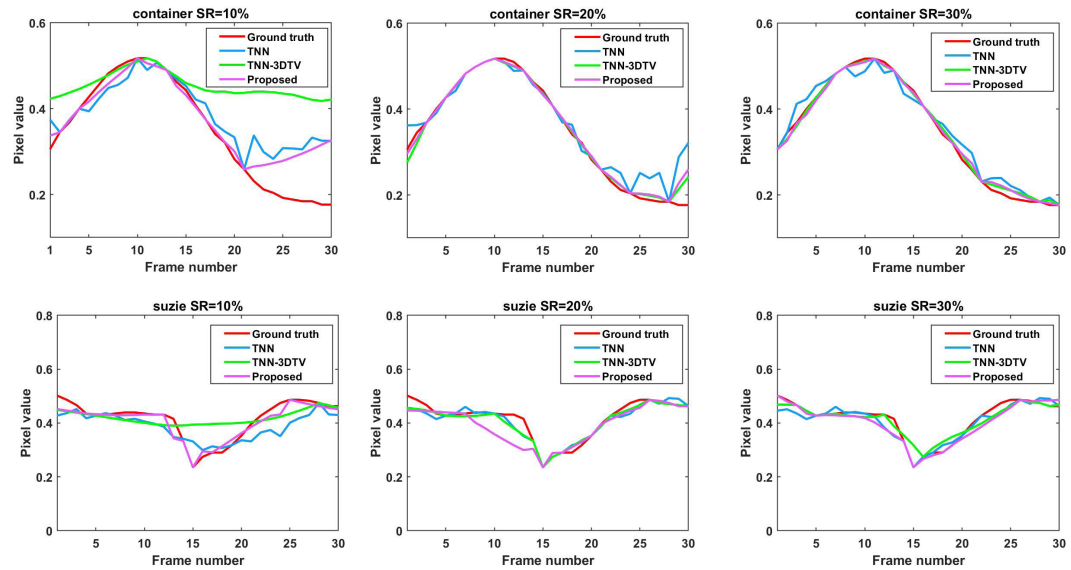


FIGURE 6. The pixel values of a selected tube of two videos recovered by TNN, TNN-3DTV, and the proposed method, respectively.

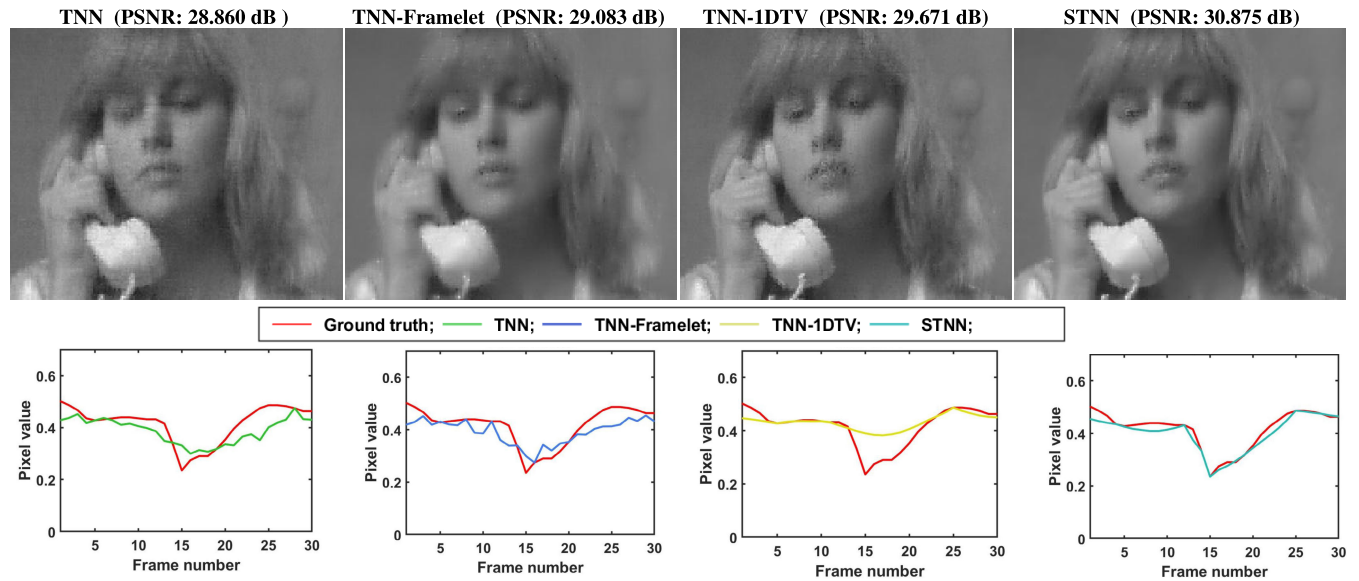


FIGURE 7. The results recovered by TNN, TNN-Framelet, TNN-1DTV, and STNN on this video with SR = 10%. The first row: A recovered frame of this video obtained by TNN, TNN-Framelet, TNN-1DTV, and STNN, respectively. The second row: The pixel values of a selected tube of the recovered video obtained by TNN, TNN-Framelet, TNN-1DTV, and STNN, respectively.

of data recovered by STNN is more similar to the curve of the original data, hence we can claim that STNN has a preferable characterization of the smooth prior along the third mode. Therefore, STNN boosts the temporal smoothness of the recovered videos, which is consistent with our motivation.

D. DISCUSSION

In this section, we discuss the role of each term in STNN and analyze parameters. To evaluate the function of each term in our model, we study the following models using the video

data *suzie* with SR = 10%:

$$\text{TNN} : \min_{\mathcal{X}} \|\mathcal{X}\|_* + \iota(\mathcal{X}),$$

$$\text{TNN-Framelet} : \min_{\mathcal{X}} \|\mathcal{X}\|_* + \lambda_1 \|W\mathcal{X}_{(3)}^T\|_{1,1} + \iota(\mathcal{X}),$$

$$\text{TNN-1DTV} : \min_{\mathcal{X}} \|\mathcal{X}\|_* + \lambda_2 \|D_s\mathcal{X}_{(3)}\|_{1,1} + \iota(\mathcal{X}).$$

Fig. 7 displays the results recovered by TNN, TNN-Framelet, TNN-1DTV, and STNN with this video *suzie*, and we can find that all components in STNN play a significative role in the performance of STNN. From the first sub-image in Fig. 7, we can observe that the TNN captures

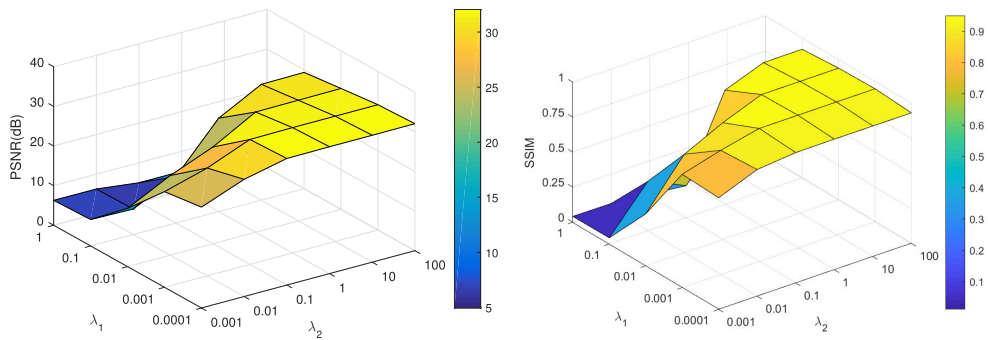


FIGURE 8. The quality metrics values with different values of parameters λ_1 and λ_2 , respectively.

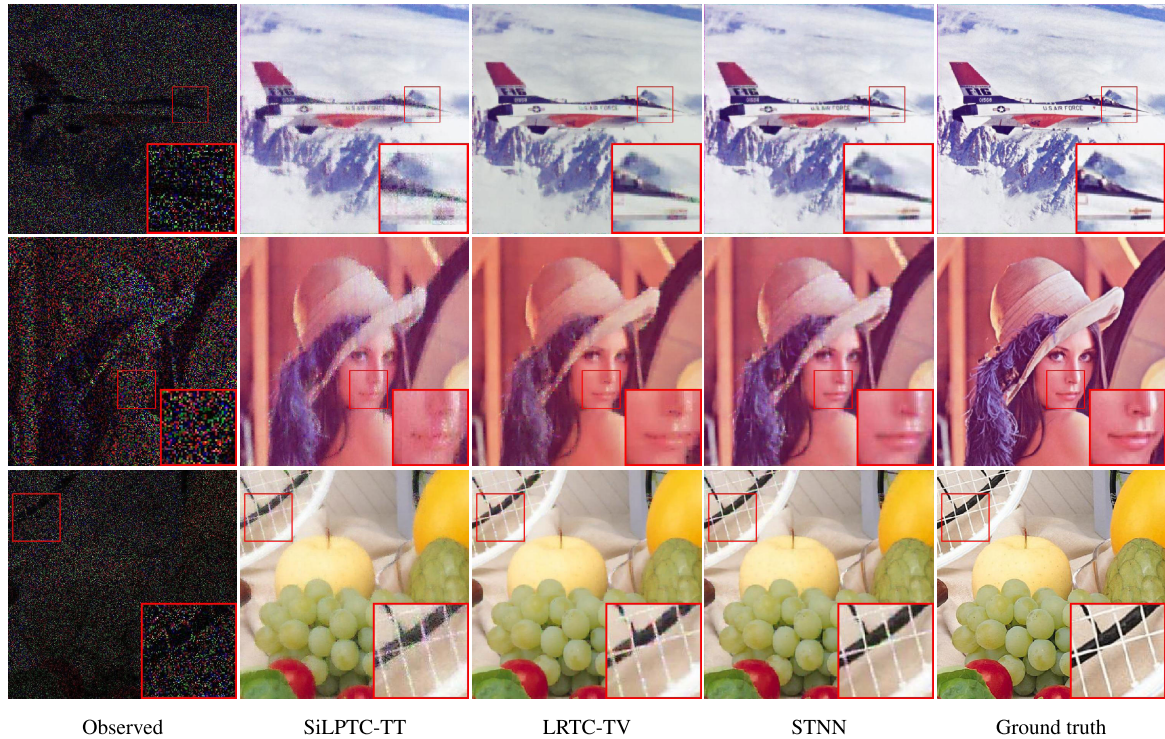


FIGURE 9. The results recovered by SiLPTC-TT, LRTC-TV, and STNN on three color images with SR = 20%.

the global information to recover the incomplete tensor. Comparing the first and the second sub-images, we can observe that the result obtained by TNN-Framelet provides more clear and sharp spatial details, which means that the framelet regularization works. Furthermore, from the second row in Fig. 7, the curve of the result obtained by TNN-1DTV, whose TV regularization along the temporal dimension, is smoother than the curve of the result obtained by TNN and TNN-Framelet, which means TV enhances the temporal smoothness of the recovered videos. It could find that STNN performs better than the competing methods, therefore, each component improves the performance of STNN.

To analyze parameters λ_1 and λ_2 , we evaluate the performance of the recovered results of the video data *container* with SR = 10%. Fig. 8 shows the change of the PSNR and SSIM values for different values of λ_1 and λ_2 . As observed,

both λ_1 and λ_2 notably affect the performance of the proposed STNN model. Moreover, Fig. 8 shows that the proposed method achieves the higher PSNR and SSIM values when $\lambda_1 = 10^{-2}$ and $\lambda_2 = 1$.

At the end of the discussion, we discuss the performance of the different tensor rank: Tucker-rank, TT rank and t-product. Therefore, we compare the proposed STNN method with two related methods: SiLPTC-TT [27] and LRTC-TV [25]. Three color images are used for the experiment, and the sampling rates (SRs) are set to be 20%, 30%, and 40%. For each SR, the PSNR and SSIM values for each completion method on three color images are listed in Table 4. It can be observed that the proposed method achieves the highest PSNR and SSIM values than SiLPTC-TT and LRTC-TV. Fig 9 shows the results recovered by these three methods with three color images

TABLE 4. The PSNR and SSIM values of different methods on three color images.

Images	SR	PSNR			SSIM		
		SiLPTC-TT	LRTC-TV	STNN	SiLPTC-TT	LRTC-TV	STNN
	20%	24.72	26.35	27.84	0.8674	0.9237	0.9346
	30%	27.39	28.87	30.64	0.9294	0.9579	0.9668
	40%	29.84	31.06	32.77	0.9606	0.9750	0.9799
	20%	24.56	26.01	26.05	0.7484	0.8061	0.8178
	30%	26.94	28.17	28.41	0.8338	0.8690	0.9424
	40%	29.30	30.04	30.34	0.8931	0.9096	0.9737
	20%	25.38	27.09	27.76	0.8552	0.8992	0.9319
	30%	27.67	29.54	30.61	0.9186	0.9413	0.9681
	40%	30.16	31.48	32.85	0.9513	0.9639	0.9807

for SR = 20%. It also can be observed that the proposed method obviously shows its visual superiority over SiLPTC-TT and LRTC-TV. The results recovered by SiLPTC-TT method have the block effects, since SiLRTC-TT method uses ket augmentation (KA) to transform a lower-order tensor into a higher-order tensor. The KA neglects the local smoothness between two nearest blocks, due to using an appropriate block structured addressing scheme. In addition, the results recovered by LRTC-TV still contain the blurry areas and miss some details. Compared with SiLPTC-TT and LRTC-TV methods, the results recovered by the proposed method preserve important tensor details well.

V. CONCLUSION

In this work, we presented a hybrid smooth regularization for restoring the incomplete tensors. Our model took advantage of TNN to preserve global information, framelet to recover details and characterize the smoothness in the spatial domain, and TV to exploit the smoothness along the third mode. To solve the STNN model, we developed an efficient ADMM algorithm. Extensive numerical results quantitatively and qualitatively demonstrated the significative performance of STNN.

REFERENCES

- [1] T. Korah and C. Rasmussen, "Spatiotemporal inpainting for recovering texture maps of occluded building facades," *IEEE Trans. Image Process.*, vol. 16, no. 9, pp. 2262–2271, Sep. 2007.
- [2] T.-X. Jiang, T.-Z. Huang, X.-L. Zhao, T.-Y. Ji, and L.-J. Deng, "Matrix factorization for low-rank tensor completion using framelet prior," *Inf. Sci.*, vols. 436–437, pp. 403–417, Apr. 2018.
- [3] B. Madathil and S. N. George, "Twist tensor total variation regularized-reweighted nuclear norm based tensor completion for video missing area recovery," *Inf. Sci.*, vol. 423, pp. 376–397, Jan. 2018.
- [4] Y. Wang, J. Peng, Q. Zhao, D. Meng, Y. Leung, and X.-L. Zhao, "Hyperspectral image restoration via total variation regularized low-rank tensor decomposition," *IEEE J. Sel. Topics Appl. Earth Observ. Remote Sens.*, vol. 11, no. 4, pp. 1227–1243, Apr. 2018.
- [5] Q.-Q. Yuan, Q. Zhang, J. Li, H.-F. Shen, and L.-P. Zhang, "Hyperspectral image denoising employing a spatial-spectral deep residual convolutional neural network," *IEEE Trans. Geosci. Remote Sens.*, vol. 57, no. 2, pp. 1205–1218, Feb. 2018.
- [6] X.-L. Zhao, F. Wang, and M. K. Ng, "A new convex optimization model for multiplicative noise and blur removal," *SIAM J. Imag. Sci.*, vol. 7, no. 1, pp. 456–475, 2014.
- [7] H. Zhang, W. He, L. Zhang, H. Shen, and Q. Yuan, "Hyperspectral image restoration using low-rank matrix recovery," *IEEE Trans. Geosci. Remote Sens.*, vol. 52, no. 8, pp. 4729–4743, Aug. 2014.
- [8] L. Zhuang and J. M. Bioucas-Dias, "Fast hyperspectral image denoising and inpainting based on low-rank and sparse representations," *IEEE J. Sel. Topics Appl. Earth Observ. Remote Sens.*, vol. 11, no. 3, pp. 730–742, Mar. 2018.
- [9] T. G. Kolda and B. W. Bader, "Tensor decompositions and applications," *SIAM Rev.*, vol. 51, no. 3, pp. 455–500, 2009.
- [10] Y. Wang, D. Meng, and M. Yuan, "Sparse recovery: From vectors to tensors," *Nat. Sci. Rev.*, vol. 5, no. 5, pp. 756–767, 2018.
- [11] X. Zhang and M. K. Ng, "A corrected tensor nuclear norm minimization method for noisy low-rank tensor completion," *SIAM J. Imag. Sci.*, vol. 12, no. 2, pp. 1231–1273, 2019.
- [12] M. K.-P. Ng, Q. Yuan, L. Yan, and J. Sun, "An adaptive weighted tensor completion method for the recovery of remote sensing images with missing data," *IEEE Trans. Geosci. Remote Sens.*, vol. 55, no. 6, pp. 3367–3381, Jun. 2017.
- [13] B. Recht, M. Fazel, and P. A. Parrilo, "Guaranteed minimum-rank solutions of linear matrix equations via nuclear norm minimization," *SIAM Rev.*, vol. 52, no. 3, pp. 471–501, 2010.
- [14] Y.-B. Zheng, T.-Z. Huang, T.-Y. Ji, X.-L. Zhao, T.-X. Jiang, and T.-H. Ma, "Low-rank tensor completion via smooth matrix factorization," *Appl. Math. Model.*, vol. 70, pp. 677–695, Jun. 2019.
- [15] X.-T. Li, X.-L. Zhao, T.-X. Jiang, Y.-B. Zheng, T.-Y. Ji, and T.-Z. Huang, "Low-rank tensor completion via combined non-local self-similarity and low-rank regularization," *Neurocomputing*, to be published. doi: [10.1016/j.neucom.2019.07.092](https://doi.org/10.1016/j.neucom.2019.07.092).
- [16] L.-B. Cui and Y. Song, "On the uniqueness of the positive Z-eigenvector for nonnegative tensors," *J. Comput. Appl. Math.*, vol. 352, pp. 72–78, May 2019.
- [17] J. D. Carroll, S. Pruzansky, and J. B. Kruskal, "CANDELINC: A general approach to multidimensional analysis of many-way arrays with linear constraints on parameters," *Psychometrika*, vol. 45, no. 1, pp. 3–24, 1980.
- [18] L. R. Tucker, "Some mathematical notes on three-mode factor analysis," *Psychometrika*, vol. 31, no. 3, pp. 279–311, 1966.
- [19] I. V. Oseledets, "Tensor-train decomposition," *SIAM J. Sci. Comput.*, vol. 33, no. 5, pp. 2295–2317, Jan. 2011.
- [20] M. E. Kilmer, K. Braman, N. Hao, and R. C. Hoover, "Third-order tensors as operators on matrices: A theoretical and computational framework with applications in imaging," *SIAM J. Matrix Anal. Appl.*, vol. 34, no. 1, pp. 148–172, 2013.
- [21] M.-Y. Zhou, Y. Liu, Z. Long, L. Chen, and C. Zhu, "Tensor rank learning in CP decomposition via convolutional neural network," *Signal Process., Image Commun.*, vol. 73, pp. 12–21, Apr. 2019.
- [22] Q. Zhao, L. Zhang, and A. Cichocki, "Bayesian CP factorization of incomplete tensors with automatic rank determination," *IEEE Trans. Pattern Anal. Mach. Intell.*, vol. 37, no. 9, pp. 1751–1763, Sep. 2015.
- [23] S. Gandy, B. Recht, and I. Yamada, "Tensor completion and low-n-rank tensor recovery via convex optimization," *Inverse Problems*, vol. 27, no. 2, p. 025010, 2011.
- [24] D. Kressner, M. Steinlechner, and B. Vandereycken, "Low-rank tensor completion by Riemannian optimization," *BIT Numer. Math.*, vol. 54, no. 2, pp. 447–468, 2014.

- [25] X.-T. Li, Y. Ye, and X. Xu, "Low-rank tensor completion with total variation for visual data inpainting," in *Proc. AAAI*, 2017, pp. 2210–2216.
- [26] J. Liu, P. Musialski, P. Wonka, and J. Ye, "Tensor completion for estimating missing values in visual data," *IEEE Trans. Pattern Anal. Mach. Intell.*, vol. 35, no. 1, pp. 208–220, Jan. 2013.
- [27] J. A. Bengua, H. N. Phien, H. D. Tuan, and M. N. Do, "Efficient tensor completion for color image and video recovery: Low-rank tensor train," *IEEE Trans. Image Process.*, vol. 26, no. 5, pp. 2466–2479, May 2017.
- [28] Y. Liu, Z. Long, and C. Zhu, "Image completion using low tensor tree rank and total variation minimization," *IEEE Trans. Multimedia*, vol. 21, no. 2, pp. 338–350, Feb. 2019.
- [29] T.-Y. Ji, T.-Z. Huang, X.-L. Zhao, T.-H. Ma, and L.-J. Deng, "A non-convex tensor rank approximation for tensor completion," *Appl. Math. Model.*, vol. 48, pp. 410–422, Aug. 2017.
- [30] Z. Zhang, G. Ely, S. Aeron, N. Hao, and M. Kilmer, "Novel methods for multilinear data completion and de-noising based on tensor-SVD," in *Proc. IEEE Conf. Comput. Vis. Pattern Recognit. (CVPR)*, Jun. 2014, pp. 3842–3849.
- [31] Z. Zhang and S. Aeron, "Exact tensor completion using t-SVD," *IEEE Trans. Signal Process.*, vol. 65, no. 6, pp. 1511–1526, Mar. 2015.
- [32] W. Hu, D. Tao, W. Zhang, Y. Xie, and Y. Yang, "The twist tensor nuclear norm for video completion," *IEEE Trans. Neural Netw. Learn. Syst.*, vol. 28, no. 12, pp. 2961–2973, Dec. 2016.
- [33] W.-H. Xu, X.-L. Zhao, T.-Y. Ji, J.-Q. Miao, T.-H. Ma, S. Wang, and T.-Z. Huang, "Laplace function based nonconvex surrogate for low-rank tensor completion," *Signal Process., Image Commun.*, vol. 73, pp. 62–69, Apr. 2019.
- [34] C.-Y. Lu, J. Feng, Y. Chen, W. Liu, Z. Lin, and S. Yan, "Tensor robust principal component analysis: Exact recovery of corrupted low-rank tensors via convex optimization," in *Proc. IEEE Conf. Comput. Vis. Pattern Recognit. (CVPR)*, Jun. 2016, pp. 5249–5257.
- [35] F. Jiang, X.-Y. Liu, H. Lu, and R. Shen, "Anisotropic total variation regularized low-rank tensor completion based on tensor nuclear norm for color image inpainting," in *Proc. IEEE Int. Conf. Acoust., Speech Signal Process. (ICASSP)*, Apr. 2018, pp. 1363–1367.
- [36] Y.-T. Wang, X.-L. Zhao, T.-X. Jiang, L.-J. Deng, T.-H. Ma, Y.-T. Zhang, and T.-Z. Huang, "A total variation and group sparsity based tensor optimization model for video rain streak removal," *Signal Process., Image Commun.*, vol. 73, pp. 96–108, Apr. 2019.
- [37] W. He, L. Yuan, and N. Yokoya, "Total-variation-regularized tensor ring completion for remote sensing image reconstruction," in *Proc. IEEE Int. Conf. Acoust., Speech Signal Process. (ICASSP)*, May 2019, pp. 8603–8607.
- [38] M.-R. Bai, X. Zhang, and Q. Shao, "Adaptive correction procedure for TVL_1 image deblurring under impulse noise," *Inverse Problems*, vol. 32, no. 8, p. 085004, 2016.
- [39] Y. Chen, S. Wang, and Y. Zhou, "Tensor nuclear norm-based low-rank approximation with total variation regularization," *IEEE J. Sel. Topics Signal Process.*, vol. 12, no. 6, pp. 1364–1377, Dec. 2018.
- [40] L. Song, B. Du, L. Zhang, and L. Zhang, "A low-rank total-variation regularized tensor completion algorithm," in *Proc. CCF Chin. Conf. Comput. Vis.*, 2017, pp. 311–322.
- [41] D. C. Dobson and F. Santosa, "Recovery of blocky images from noisy and blurred data," *SIAM J. Appl. Math.*, vol. 56, no. 4, pp. 1181–1198, 1996.
- [42] M. Nikolova, "Local strong homogeneity of a regularized estimator," *SIAM J. Appl. Math.*, vol. 61, pp. 633–658, Feb. 2000.
- [43] J.-H. Yang, X.-L. Zhao, J.-J. Mei, S. Wang, T.-H. Ma, and T.-Z. Huang, "Total variation and high-order total variation adaptive model for restoring blurred images with cauchy noise," *Comput. Math. Appl.*, vol. 77, no. 5, pp. 1255–1272, 2019.
- [44] J.-H. Yang, X.-L. Zhao, T.-H. Ma, Y. Chen, T.-Z. Huang, and M. Ding, "Remote sensing images destriping using unidirectional hybrid total variation and nonconvex low-rank regularization," *J. Comput. Appl. Math.*, vol. 363, pp. 124–144, 2020.
- [45] J.-F. Cai, R. H. Chan, and Z. Shen, "A framelet-based image inpainting algorithm," *Appl. Comput. Harmon. Anal.*, vol. 24, no. 2, pp. 131–149, Mar. 2008.
- [46] J.-F. Cai, B. Dong, S. Osher, and Z. Shen, "Image restoration: Total variation, wavelet frames, and beyond," *J. Amer. Math. Soc.*, vol. 25, no. 4, pp. 1033–1089, 2012.
- [47] A. Ron and Z. Shen, "Affine systems in $L_2(\mathcal{R}^d)$: The analysis of the analysis operator," *J. Funct. Anal.*, vol. 148, no. 2, pp. 408–447, 1997.
- [48] J.-F. Cai, B. Dong, and Z. Shen, "Image restoration: A wavelet frame based model for piecewise smooth functions and beyond," *Appl. Comput. Harmon. Anal.*, vol. 41, no. 1, pp. 94–138, 2016.
- [49] M.-M. Cheng, L. Jing, and M. K. Ng, "Tensor-based low-dimensional representation learning for multi-view clustering," *IEEE Trans. Image Process.*, vol. 28, no. 5, pp. 2399–2414, May 2019.
- [50] L.-B. Cui, M.-H. Li, and Y. Song, "Preconditioned tensor splitting iterations method for solving multi-linear systems," *Appl. Math. Lett.*, vol. 96, pp. 89–94, Oct. 2019.
- [51] Z. Wang, A. C. Bovik, H. R. Sheikh, and E. P. Simoncelli, "Image quality assessment: From error visibility to structural similarity," *IEEE Trans. Image Process.*, vol. 13, no. 4, pp. 600–612, Apr. 2004.



XI-LE ZHAO received the M.S. and Ph.D. degrees from the University of Electronic Science and Technology of China (UESTC), Chengdu, China, in 2009 and 2012, respectively, where he is currently a Professor with the School of Mathematical Sciences. His research interests include the sparse and low-rank modeling for image processing problems.



XIN NIE received the B.S. degree in information and computing science from Sichuan Agricultural University, Ya'an, China, in 2018. She is currently pursuing the master's degree with the School of Mathematical Sciences, University of Electronic Science and Technology of China, Chengdu, China. Her research interests include tensor analysis and high dimensional image processing.



YU-BANG ZHENG received the B.S. degree in information and computing science from the Anhui University of Finance and Economics, Bengbu, China, in 2017. He is currently pursuing the Ph.D. degree with the School of Mathematical Sciences, University of Electronic Science and Technology of China, Chengdu, China. His current research interests include sparse and low-rank modeling for image processing problems. More information can be found on his homepage <http://www.escience.cn/people/YuBangZheng/index.html>.



TENG-YU JI received the B.S. and Ph.D. degrees from the School of Mathematical Sciences, University of Electronic Science and Technology of China, Chengdu, China, in 2012 and 2018, respectively. He is currently an Assistant Professor with the Department of Applied Mathematics, Northwestern Polytechnical University, Xi'an, China. His research interests include tensor decomposition and applications, including tensor completion and remotely sensed image reconstruction.



TING-ZHU HUANG received the B.S., M.S., and Ph.D. degrees in computational mathematics from the Department of Mathematics, Xi'an Jiaotong University, Xi'an, China. He is currently a Professor with the School of Mathematical Sciences, University of Electronic Science and Technology of China, Chengdu, China. His research interests include scientific computation and applications, numerical algorithms for image processing, numerical linear algebra, preconditioning technologies, and matrix analysis with applications. He is also an Editor of *The Scientific World Journal*, *Advances in Numerical Analysis*, the *Journal of Applied Mathematics*, the *Journal of Pure and Applied Mathematics*, *Advances in Applied Mathematics*, and the *Journal of Electronic Science and Technology*, China.